Chemical Science

ROYAL SOCIETY OF CHEMISTRY

EDGE ARTICLE

View Article Online
View Journal | View Issue

Cite this: *Chem. Sci.*, 2024, **15**, 3721

All publication charges for this article have been paid for by the Royal Society of Chemistry

Received 14th December 2023
Accepted 29th January 2024

DOI: 10.1039/d3sc06710f

rsc.li/chemical-science

Regulating luminescence thermal enhancement in negative thermal expansion metal–organic frameworks†

Liang Chen,[a] Yili Cao,*[a] Rui Ma,[a] Hongmei Cao,[a] Xin Chen,[a] Kun Lin,[a] Qiang Li,[a] Jinxia Deng,[a] Chunyu Liu,[b] Yilin Wang,[c] Ling Huang*[c] and Xianran Xing*[a]

Overcoming thermal quenching is generally essential for the practical application of luminescent materials. It has been recently found that frameworks with negative thermal expansion (NTE) could be a promising candidate to engineer unconventional luminescence thermal enhancement. However, the mechanism through which luminescence thermal enhancement can be well tuned remains an open issue. In this work, enabled by altering ligands in a series of UiO-66 derived Eu-based metal–organic frameworks, it was revealed that the changes in the thermal expansion are closely related to luminescence thermal enhancement. The NTE of the aromatic ring part favors luminescence thermal enhancement, while contraction of the carboxylic acid part plays the opposite role. Modulation of functional groups in ligands can change the thermal vibration of aromatic rings and then achieve luminescence thermal enhancement in a wide temperature window. Our findings pave the way to manipulate the NTE and luminescence thermal enhancement based on ligand engineering.

Introduction

Luminescent materials are an attractive research objective in materials science for their abundant applications in organic light-emitting diodes (OLEDs),[1,2] biological analysis, imaging,[3,4] sensors,[5,6] *etc.* However, thermal quenching (TQ) is generally unavoidable, which leads to the degradation of their luminescence performances.[7–9] How to maintain the emission intensity with increasing temperature and thus overcome TQ has become an urgent issue, which not only can reduce energy loss, but also broadens the temperature range for luminescence applications.

Recently, negative thermal expansion (NTE) in framework materials that defies common sense has shown potential applications in overcoming TQ.[10–15] The atomic distances in the lattice of NTE materials paradoxically contract with increasing temperature,[16–19] which facilitates the modulation of charge transfer paths and then achieves the maintenance or even enhancement of luminescence intensity. Although NTE provides ideas to overcome thermal quenching, how to modulate NTE to tailor luminescence thermal enhancement is a fledgling research topic. Previously, we reported the NTE behaviour leading to significant thermal enhancement of luminescence in molecular materials,[20] which is based on the principle that NTE facilitates an improved ligand-to-metal charge transfer (LMCT) path. It is reasonable to speculate that improving the LMCT process by modulating NTE is the key to achieving tailored luminescence thermal enhancement.

Metal–organic frameworks (MOFs)[21–23] are an ideal platform for investigating the modulation of NTE to overcome TQ due to their well-defined space location and flexible and tuneable structure,[24–27] outstanding luminescence properties,[28] as well as considerable NTE intensity.[17,29] The UiO-66 family is one of the most investigated MOFs.[30] The combination of different metal nodes and various forms of linear carboxylic acid ligands constructs a large number of UiO-66 derivatives, which have excellent stability and can be competent for most practical applications.[31] Furthermore, under illumination, the UiO-66 family generally has a typical LMCT process,[32] which is suitable for achieving luminescence thermal enhancement through NTE. As an important structure modulation approach, ligand engineering has been widely used in the application fields of MOFs including gas adsorption and separation and catalysis.[33,34] It can promote targeted properties by tailoring the functional groups of ligands in MOFs without changing their crystal topology, and thus offer us an ideal design approach to property modulation.

Herein, we synthesized a series of UiO-66 derived Eu-based MOFs (Eu-NH_2-BDC, Eu-OH-BDC, and Eu-NDC) to correlate

---

[a] *Beijing Advanced Innovation Center for Materials Genome Engineering, Institute of Solid State Chemistry, University of Science and Technology Beijing, 100083, Beijing, China. E-mail: xing@ustb.edu.cn; yilicao@ustb.edu.cn*

[b] *Department of Chemistry, Key Laboratory of Organic Optoelectronics and Molecular Engineering of the Ministry of Education, Tsinghua University, 100084, Beijing, China*

[c] *Institute of Advanced Materials, Nanjing Tech University, 211816, Nanjing, China. E-mail: iamlhuang@njtech.edu.cn*

† Electronic supplementary information (ESI) available: Experimental and additional characterization. CCDC 2246487–2246501. For ESI and crystallographic data in CIF or other electronic format see DOI: **https://doi.org/10.1039/d3sc06710f**

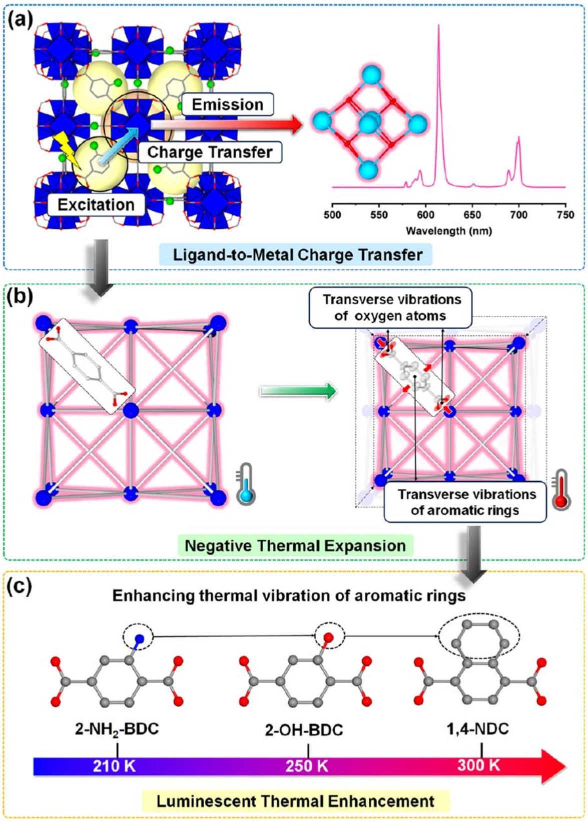

Fig. 1 Schematic illustration of UiO-66 derived Eu-based MOFs modulating NTE through ligand engineering to achieve an increased range of luminescence thermal enhancement. (a) The charge transfer path of the MOF under illumination. All hydrogens are omitted for clarity. (Colour code: Eu, sky blue; O, red; C, grey; functional group, green). (b) NTE originates from the synergy of the transverse vibrations of both the oxygen atom and the aromatic ring parts of the ligand. (c) Ligands with different functional group modifications, which results in a sequential increase in the range of luminescence thermal enhancement.

their NTE and luminescence relationships, and ligand engineering was also involved to explore the effect of different functional groups (Fig. 1a). All three MOFs exhibit significant NTE and luminescence thermal enhancement behaviours. Optical measurements indicate that luminescence comes from the typical LMCT process (Fig. 1b). Precise structure analysis indicates that thermal expansion changes in structures are dominated by the thermal vibrations of aromatic rings and oxygen atoms in ligands (Fig. 1c). The different thermal vibrations dominate their NTE behaviours and manipulate the luminescence intensity in the temperature window. Moreover, different functional groups in ligands were found to affect the aromatic vibration and then have an essential influence on their NTE behaviours and luminescent properties.

Methods

Materials

All chemicals were used without any further purification. 2-aminoterephthalic acid (2-NH_2-BDC), 2-hydroxyterephthalic acid (2-OH-BDC), 1,4-naphthalenedicarboxylate (1,4-NDC), europium nitrate hexahydrate and 2-fluorobenzoic acid (2-FBA) were purchased from Macklin. DMA and other materials were purchased from Aladdin.

Synthesis of Eu-NH_2-BDC, Eu-OH-BDC, and Eu-NDC activated crystals

$Eu(NO_3)_3 \cdot 6H_2O$ (19.4 mg, 0.044 mmol), 2-NH_2-BDC (8 mg, 0.044 mmol) and 2-FBA (110 mg, 0.7 mmol) were added to the solution of DMA (2 ml) in a 4 ml scintillation vial, forming a suspension solution using an ultrasound method, sealed, and heated to 120 °C in 2 h; the temperature was held for 72 h and then cooled to room temperature in 2 h. The colourless octahedral crystals of Eu-NH_2-BDC were collected *via* centrifugation and washed three times with DMF (3 × 20 ml) and three times with methanol (3 × 20 ml). All the crystals were soaked in methanol for at least 3 days for solvent exchange and dried in a vacuum at 100 °C overnight. Eu-OH-BDC and Eu-NDC were synthesized using the same method, and only the ligands were replaced with 2-OH-BDC (8 mg, 0.044 mmol) and 1,4-NDC (9.5 mg, 0.044 mmol), respectively.

Variable temperature optical measurements

Excitation spectra were collected by using an Edinburgh FLS1000 spectrofluorometer (Edinburgh Instruments Ltd) equipped with a continuous xenon lamp (450 W) as an excitation source; the optimal excitation wavelengths are 360 nm (Eu-NH_2-BDC), 394 nm (Eu-OH-BDC), and 394 nm (Eu-NDC), respectively. The temperature-dependent solid state luminescence spectra were obtained on the same spectrophotometer at controlled variable temperature (80–400 K with an interval of 10 K) and were recorded with an Oxford Instruments liquid nitrogen cryostat accessory. The time decay curves were measured under the same conditions, with a temperature range of 100–300 K. The average lifetime was obtained from the double-exponential decays according to equation:

$$\tau_{\text{avg}} = \frac{\sum A\tau^2}{\sum A_i\tau_i}, \quad i = 1, 2$$

where τ is the decay time of luminescence intensity and A_i is the amplitude of each component.

Photoluminescence quantum yield (PLQY) measurements

The photoluminescence quantum yield measurements were recorded using an integrated sphere, which was attached to the FLS1000 spectrofluorometer. The PLQY was calculated using the equation: $\eta_{QY} = I_S/(E_R - E_S)$, in which I_S represents the luminescence emission spectrum of the sample, E_R is the spectrum of the excitation light from the empty integrated sphere (without the sample), and E_S is the excitation spectrum for exciting the sample.

Differential scanning calorimetry (DSC) analysis

DSC traces were obtained with a Discovery 250 DSC apparatus. The samples (about 6 mg) were heated at rates of 5 °C min^{-1} from −165 to 127 °C under a helium flow of 20 ml min^{-1}.

Variable-temperature powder X-ray diffraction

XRD patterns of the sintered samples were obtained using a laboratory diffractometer (PANalytical X'PertIII, Holland, Cu Kα radiation, $\lambda = 1.5406$ Å). Low-temperature powder X-ray diffraction patterns were collected in the same diffractometer and an Anton Par TTK 400 low-temperature attachment was used. XRD data were collected from −150–100 °C over a 2θ range from 5 to 50°. The heating rate was 10 °C min^{-1}, and the sample was held for 5 min at a specified temperature to reach heating equilibrium. After the first round of measurements, the samples were cooled down directly to −150 °C for the second round of variable temperature measurements without removing them. The data were refined using the Rietveld refinement method using FULLPROF software.

Variable-temperature single-crystal X-ray diffraction

Single-crystal diffraction data were collected using a Rigaku XtaLAB Synergy Custom diffractometer with Mo $K\alpha = 0.71073$ Å at 100, 150, 200, 250, and 300 K. Structure solution and refinement were performed using SHELXL using Olex2 software. Crystal information and details related to the structural refinements are presented in ESI Tables 8–10.† Variable temperature crystallographic data for Eu-based MOF structures have been deposited in the Cambridge Crystallographic Data Centre (CCDC) with numbers 2246487–2246501.

Variable-temperature FT-IR measurements

The FTIR spectra were obtained by the KBr pellet method on a Bruker Vertex V80V Vacuum FTIR spectrometer with a spectral range of 650–4000 cm^{-1} and resolution of 2 cm^{-1} and 128 scans. The KBr pellets were transferred into a vacuum cell with an Oxford closed-cycle cryostat, equipped with KBr windows and placed at the focal point of the sample compartment of the infrared spectrometer. The measurements were performed by cooling and heating the KBr pellets in the temperature range of 100–300 K. The temperature was regulated using a MercuriTC temperature controller and the vacuum inside the cryostat was 10^{-4} mbar.

Results and discussion

Synthesis and crystal structure

The series of isomeric Eu-based MOFs were synthesized according to previous references with slight modifications.[35–37] In order to exclude the effect of solvent, the obtained pre-synthesized crystals were soaked in methanol for three days and replaced with methanol once a day, and then vacuumed at 373 K for 24 h. The structures of the activated crystals were obtained by single-crystal X-ray diffraction (SCXRD) analysis. The phase purity of the activated samples was confirmed by powder X-ray diffraction (PXRD) patterns (Fig. S1†).

We described Eu-NH_2-BDC in detail because these three compounds were isomorphic and only different in functional groups of the ligands. The results of SCXRD indicated that Eu-NH_2-BDC crystallizes in the cubic $Fm\bar{3}m$ space group. Each Eu^{3+} atom forms a nine-coordination configuration with four μ_3-OH, four O atoms from four different carboxylic acid groups, and a water molecule. The six adjacent Eu^{3+} atoms are constructed into a 12-connected molecular building block by μ_3-OH and completely deprotonated carboxylic groups. The adjacent blocks are connected by ligand bridges to form two types of polyhedral cages, which are finally packed into a three-dimensional (3D) network (Fig. S2†).

Photophysical properties

Lanthanide MOFs are considered one of the most potential luminescent materials for their unique spectral properties such as typical sharp characteristic spectra, good stability and tuneable photophysical properties.[38,39] The solid-state emission spectra of Eu-based MOFs in Fig. 2a show that they exhibit similarly fine structured characteristic emission with a narrow maximum emission peak at around 614 nm which can be attributed to the $^5D_0 \rightarrow {}^7F_2$ emission band from the Eu atom.[40–44] The excitation spectra of these MOFs and their corresponding ligands are overlapping, but the emission spectra of these MOFs contain only the characteristic emission from the Eu^{3+} ion (Fig. S3†), indicating a typical antenna effect in the system,[45,46] that is, a charge transfer process from the ligand to the metal center (LMCT). The $\pi \rightarrow \pi^*$ transition of the ligand is excited, followed by intersystem crossing (ISC) to the triplet state, and through energy transfer (ET) to the Eu^{3+} ion for emission[47] (Fig. 2b).

Variable-temperature solid-state luminescence was measured to investigate the change in emission intensity with temperature. We found that the emission positions of the three compounds did not change with temperature, indicating that the emission process is stable. Interestingly, they both exhibit two types of luminescence behaviours, that is, thermal enhancement in a certain temperature range and subsequent TQ. A sequentially increasing temperature range of thermal enhancement among the three MOFs has been observed, that is 80–200 K for Eu-NH_2-BDC, 80–250 K for Eu-OH-BDC, and 80–300 K for Eu-NDC (the luminescence intensity stabilization part is also included in the thermal enhancement), respectively (Fig. 2c). Eu-NH_2-BDC showed the strongest thermal enhancement at 140 K with an enhancement of 20.5%, while both Eu-OH-BDC and Eu-NDC have their strongest luminescence intensity at 170 K with an enhancement of 35.9% and 14.9%. Further cycling experiments demonstrated the reversibility of these thermal enhancement processes (Fig. S4–6†). Moreover, we also measured the temperature dependence of the lifetimes of the three Eu-based MOFs (Fig. S7†). Their lifetimes are maintained within the range of a few hundred microseconds (Fig. 2d). In general, nonradiative relaxation increases significantly along with increasing temperature, resulting in a rapid decay of luminescent lifetimes. However, the decay of the three compounds appears significantly different (Fig. 2e). In Eu-NH_2-BDC, lifetime decays slowly in the thermal enhancement temperature range and decays rapidly in the TQ temperature range. The lifetime decay of Eu-OH-BDC is much weaker than that of Eu-NH_2-BDC, and the least lifetime decay appears in Eu-NDC, which even showed a paradoxical enhancement. Considering that the emission from the Eu^{3+} ion is relatively stable, the weaker or even paradoxical enhancement of the lifetime decay

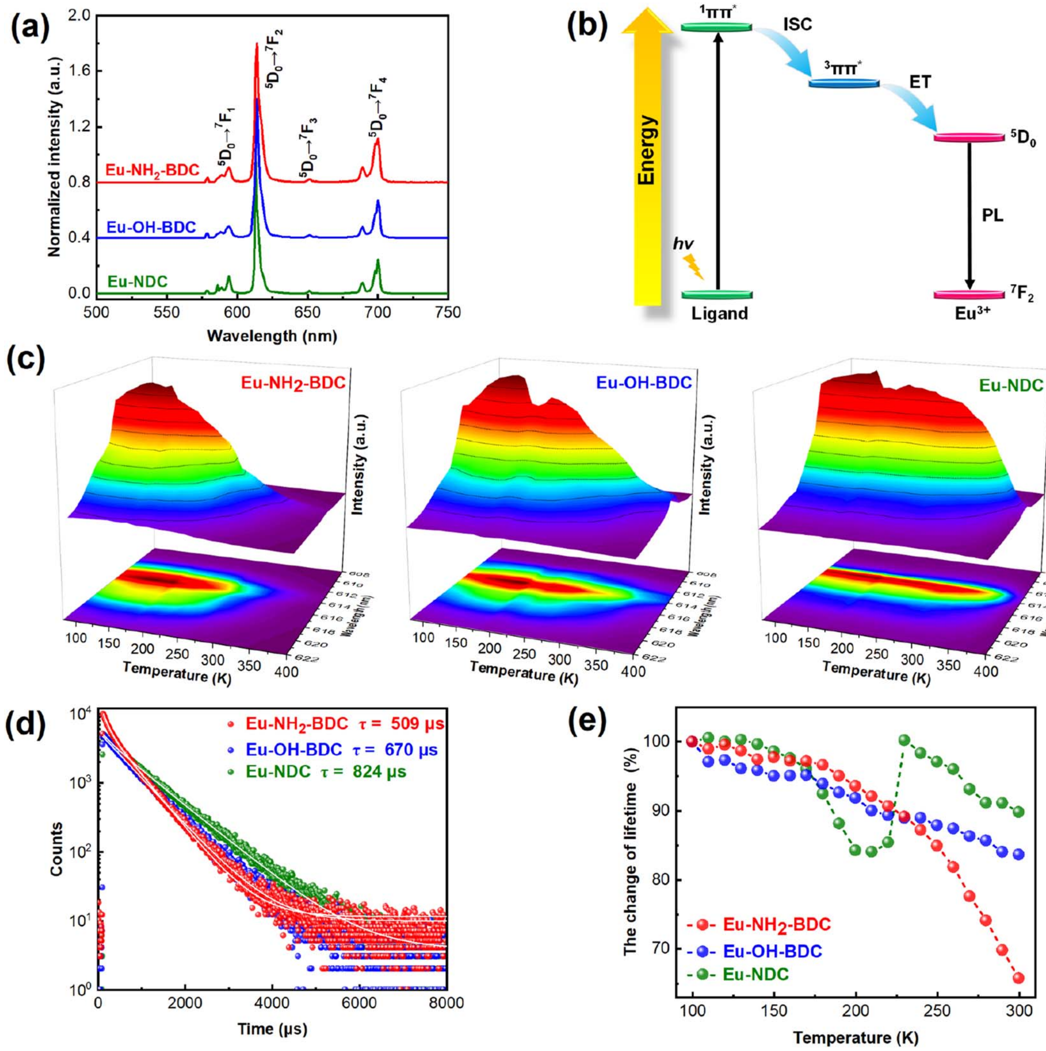

Fig. 2 Variable-temperature optical properties. (a) The emission spectra of Eu-NH_2-BDC, Eu-OH-BDC, and Eu-NDC. (b) Schematic diagram of the energy transfer process in three Eu-based MOFs. (c) Intensity variation of the maximum emission peak with temperature in Eu-NH_2-BDC, Eu-OH-BDC, and Eu-NDC. (d) Lifetime decay of the three Eu-based MOFs at 100 K. (e) Temperature-dependence of lifetimes of the three Eu-based MOFs.

in Eu-NDC may reflect the improvement of the charge transfer process. Moreover, their photoluminescence quantum yields (PLQYs) at room temperature were tested to be 0.35% (Eu-NH_2-BDC), 1.92% (Eu-OH-BDC), and 5.67% (Eu-NDC), respectively (Table S1†), which indicates that the luminescence efficiency also improves combined with a relatively wider thermal enhancement temperature range.

Negative thermal expansion behaviors

Differential scanning calorimetry (DSC) thermal cycling experiments of the three MOFs (Fig. S8†) showed no absorption and exothermic peaks, which suggests that their abnormal luminescence thermal enhancement behaviours have no relationship with the phase transition. To investigate the temperature-dependent structural changes of Eu-NH_2-BDC, Eu-OH-BDC, and Eu-NDC, variable temperature powder X-ray diffraction (VT-PXRD) measurements were performed (Fig. S9–11†). No phase transition was observed in the measured temperature range of 123–373 K. The lattice parameters were obtained by the Rietveld refinement method[48] (Fig. S12 and Tables S2–4†). All three compounds exhibit nonlinear NTE behaviour with increasing temperature, which is consistent with further cyclic VT-PXRD results (Fig. S13–17 and Tables S5–7†), indicating that the NTE behaviours of the three MOFs are reversible. By comparing their NTE behaviours and luminescence intensity with temperature (Fig. 3), we found that the NTE progress of the three MOFs could also be divided into two parts. In the low temperature part, the NTE coefficients are $\alpha_a = +4.86 \times 10^{-6}\ \mathrm{K}^{-1}$ for Eu-NH_2-BDC (from 123 to 203 K), $\alpha_a = -13.79 \times 10^{-6}\ \mathrm{K}^{-1}$ for Eu-OH-BDC (from 123 to 243 K), and $\alpha_a = -3.93 \times 10^{-6}\ \mathrm{K}^{-1}$ for Eu-NDC (from 123 to 303 K), respectively. NTE is weak and corresponds to luminescence thermal enhancement. In the high temperature part, the NTE coefficients are $\alpha_a = -30.43 \times 10^{-6}\ \mathrm{K}^{-1}$ for Eu-NH_2-BDC (from 203 to 373 K), $\alpha_a = -30.95 \times 10^{-6}\ \mathrm{K}^{-1}$ for Eu-OH-BDC (from 243 to 373 K), and $\alpha_a = -23.31 \times 10^{-6}$ for Eu-NDC (from 303 to 373 K), respectively. NTE is significantly enhanced but corresponds to TQ.

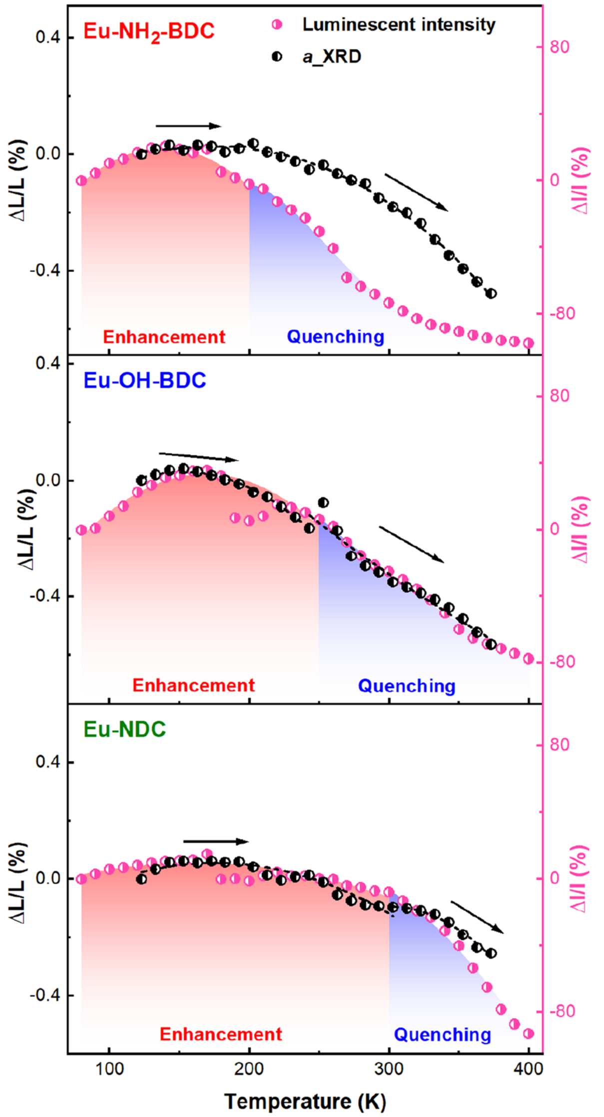

Fig. 3 Luminescence intensity corresponding to the change in NTE. Temperature-dependent lattice parameter and luminescence intensity changes of Eu-NH$_2$-BDC, Eu-OH-BDC, and Eu-NDC. The thermal enhancement part (red) and TQ part (blue) are marked with different colours.

To clarify the connection between luminescence thermal enhancement and NTE, it is essential to analyse the origin of the NTE. We performed variable temperature single crystal X-ray diffraction (VT-SCXRD) to get precise structural changes, and the refined results are in good agreement with the general trend of VT-PXRD (Tables S8–10 and Fig. S18†). The structures of the three MOFs are constructed by the europium oxygen cluster and ligand, and their lengths decide the size of the unit cell. Length changes of the europium oxygen cluster (d1), the ligand (d2) and the unit cell (*a*) with temperature are shown in Fig. 4a. We found that thermal expansion of the structure is controlled by both d1 and d2, but the change in d1 is minor while d2 is more consistent with the change in thermal expansion, indicating that the thermal expansion of the framework is mainly controlled by the ligand.

The atomic thermal vibrations of the crystal structure (Fig. S19†) were further analysed and showed that the direction of maximum atomic thermal vibration in ligands is perpendicular to the ligand plane and corresponds to the transverse vibration of ligands, which then results in NTE along the ligand direction. As shown in Fig. 4b, the transverse vibration of the ligand could be divided into the aromatic ring and oxygen atoms, and their different transverse vibrations were analysed using the change of length of these two parts (d3 and d4, dominated by thermal vibrations of oxygen atoms and aromatic rings, respectively) to evaluate their contribution to thermal expansion. Interestingly, d3 and d4 exhibit opposite trends with temperature in nonlinear modes, which corresponds to the change in thermal expansion of the framework. The thermal expansion change of d3 determines the thermal expansion of the framework significantly. In low temperature ranges, the positive thermal expansion of the framework mainly originates from the positive thermal expansion of d3, and when d3 transitions to NTE, the framework also transfers to NTE.

Due to the remarkable LMCT character of this series Eu-based MOFs, the change of the ligand with temperature could inevitably affect the charge transfer. In this work, the change in thermal expansion of the framework corresponds to the change in luminescence intensity. As direct reflection indices of thermal expansion in ligands, d3 and d4 could directly correlate with luminescence thermal enhancement. The NTE of the aromatic ring typically facilitates charge transfer;[20] the larger the NTE of d4, the greater the percentage of luminescence thermal enhancement (35.9% for Eu-OH-BDC, 20.5% for Eu-NH$_2$-BDC and 14.9% for Eu-NDC, respectively). Moreover, when the thermal expansion of d3 decays or even transfers to NTE, which indicates the increasing transverse vibrations of the oxygen atoms, a rapid attenuation of the luminescence intensity can be observed.

As the direct coordinated site linking Eu metals, O atoms play key roles in the LMCT progress, and the increasing vibration of O atoms may have a negative effect on the LMCT progress and thus leads to a decrease in luminescence intensity. Related research is underway in our lab. Moreover, different functional groups can affect the transverse vibrations of the aromatic ring (Fig. 4c). In detail, ligands with –OH units allow the framework to show a larger NTE than –NH$_2$, combined with an increase in both the ratio and range of luminescence enhancement. The ligand in Eu-NDC with more atoms and large steric hindrance slows a later transfer temperature of thermal expansion, resulting in the largest range of luminescence thermal enhancement.

Temperature-dependent FT-IR study

There is a correlation between infrared vibration mode intensity and thermal expansion,[49,50] and we chose precise temperature-dependent Fourier transform infrared (FT-IR) spectroscopy to assist in demonstrating the correlation between vibrations and NTE. Fig. 5a–c show that the infrared spectra are dominated mostly by the characteristic bands of the ligands. In Eu-NH$_2$-BDC, the infrared peaks at 1383 cm^{-1} and 1572 cm^{-1} are attributed to the symmetric and

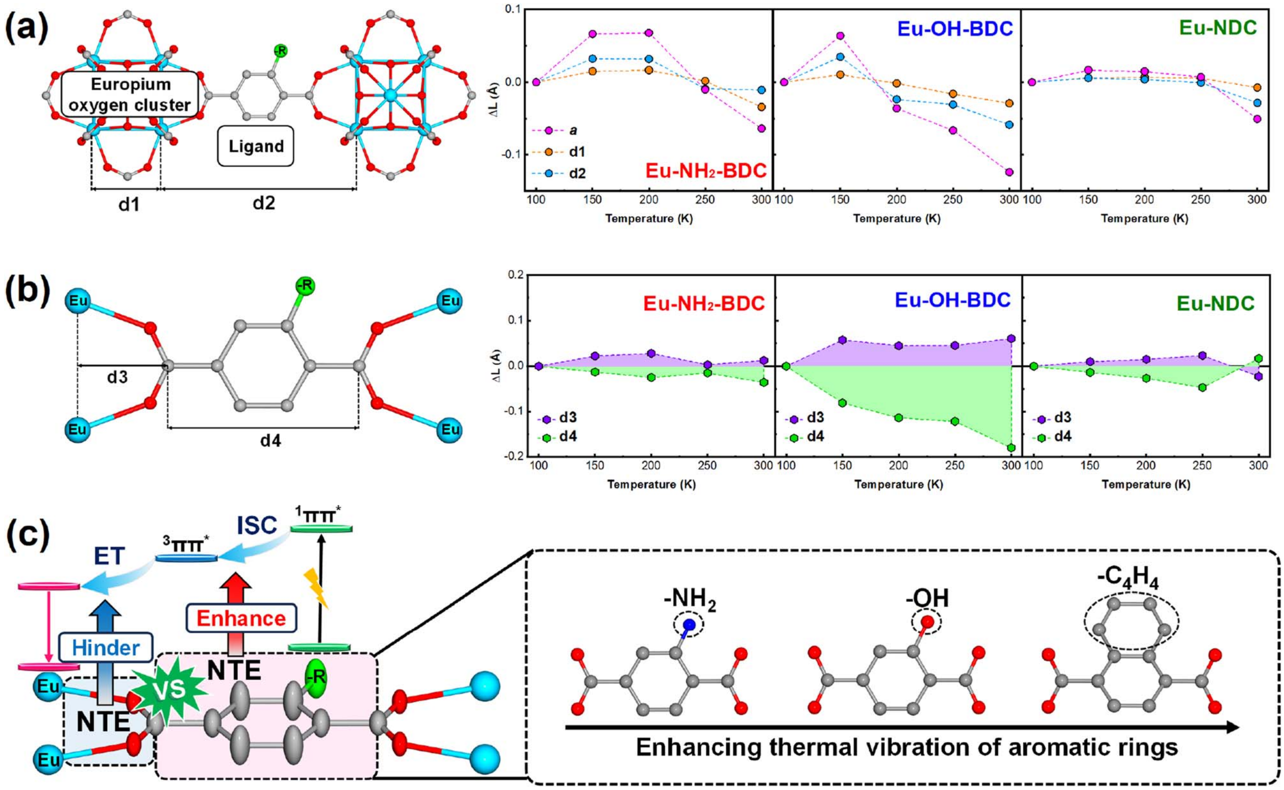

Fig. 4 NTE and luminescence thermal enhancement. The structure variation with temperature was obtained from VT-SCXRD. (a) Temperature dependent length changes of unit cell (*a*), europium oxygen cluster (d1) and ligand (d2) in Eu-NH_2-BDC, Eu-OH-BDC, and Eu-NDC. (b) Temperature dependent horizontal length of carboxylic acids (d3) and aromatic rings (d4) in Eu-NH_2-BDC, Eu-OH-BDC, and Eu-NDC. (c) Schematic mechanism of functional group modifications affecting luminescence thermal enhancement.

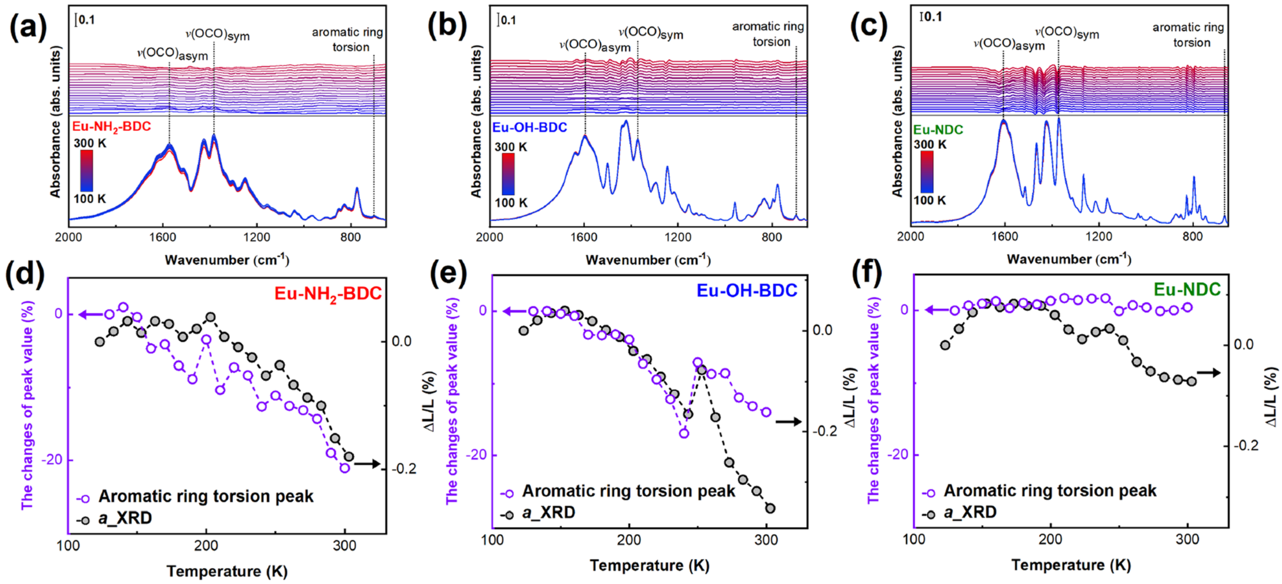

Fig. 5 Temperature-dependent molecular vibration spectroscopy. (a)–(c) FT-IR spectra (bottom panel) of Eu-NH_2-BDC, Eu-OH-BDC, and Eu-NDC in the temperature range of 100–300 K. Difference spectra (top panel) at elevated temperatures (110–300 K), each referenced to the spectrum collected at 100 K. (d)–(f) Comparison of intensity changes of peaks corresponding to aromatic ring torsion with the trend of lattice changes in Eu-NH_2-BDC, Eu-OH-BDC, and Eu-NDC.

asymmetric stretching vibration modes of –COO groups, and the peak at 702 cm^{-1} in the low frequency band comes from the aromatic ring torsion vibrations.[51–53] The symmetric stretching vibrations peak of –COO are observed at 1597 cm^{-1} and 1609 cm^{-1} in Eu-OH-BDC and Eu-NDC, respectively, while the asymmetric vibration peaks are all at 1371 cm^{-1}. The aromatic ring torsion gave peaks at 698 cm^{-1} for Eu-OH-BDC and 665 cm^{-1} for Eu-NDC. To our surprise, the intensity of peaks belonging to aromatic ring torsion was found to show a more significant change with temperature compared to other peaks (Fig. S20†). These intensity changes are consistent with the NTE trend, which indicates that the aromatic ring plays a key role in the NTE process (Fig. 5d–f). It is worth noting that in Eu-NH_2-BDC and Eu-OH-BDC, the intensity changes of the low-frequency vibration fitted well with the NTE trend, while the two trends are incommensurable in Eu-NDC, and this displacement may come from the larger steric effect and more atoms in NDC ligands.

Conclusions

In summary, we illustrate the relationship between NTE and luminescence thermal enhancement in a series of Eu-based MOFs. Precise structural determination demonstrates that the NTE of the aromatic ring facilitates luminescence thermal enhancement, yet the transverse thermal vibration of the oxygen atoms hinders charge transfer and leads to quenching. Moreover, functional group modifications with large steric hindrance in ligands can improve the thermal vibration of the aromatic ring and thus broaden the temperature range of thermal enhancement. The NTE-luminescence correlation and ligand engineering approach in this work provides insightful guidance in terms of overcoming TQ with NTE molecular materials.

Data availability

CCDC 2246487–2246501 contain the supplementary crystallographic data for this paper. These data can be obtained free of charge *via* **https://www.ccdc.cam.ac.uk/data_request/cif**, or by emailing data_request@ccdc.cam.ac.uk, or by contacting The Cambridge Crystallographic Data Centre, 12 Union Road, Cambridge CB2 1EZ, UK; fax: +44 1223 336033. The data that support the findings of this study are available from the corresponding author. Besides, source data are provided with this paper.

Author contributions

X. X. designed and guided the project. L. C., R. M., and H. C. synthesized the materials. L. C. performed the majority of the experiments as well as data analysis. C. L. assisted in collecting the single crystal X-ray diffraction data and solved the structures. L. C. drafted the paper. X. C., K. L., Q. L., J. D., and Y. W. provided important advice on data analysis. C. L., Y. C., L. H., and X. X. wrote the manuscript with contributions from all the authors.

Conflicts of interest

There are no conflicts to declare.

Acknowledgements

This research was supported by the National Key R&D Program of China (2020YFA0406202), the National Natural Science Foundation of China (22090042, 21731001 and 21971009), the Program for Changjiang Scholars, the Innovative Research Team in University (grant no. IRT1207), and the Program of Introducing Talents of Discipline to Universities (grant no. B14003). We thank Prof. Zi-Shuo Yao, Dr Ling-Tai Yue, and Dr Yu-Xia Li, Beijing Institute of Technology, for single-crystal X-ray measurement. We thank staff at the X-ray crystallography platform of the Tsinghua University Technology Center for Protein Research for providing facility support. We thank the staff from the BL06B1 beamline of the Shanghai Synchrotron Radiation Facility (SSRF) for assistance during IR data collection (No. 2022-SSRF-JJ-500237).

Notes and references

1 M. Pan, W. M. Liao, S. Y. Yin, S. S. Sun and C. Y. Su, Single-Phase White-Light-Emitting and Photoluminescent Color-Tuning Coordination Assemblies, *Chem. Rev.*, 2018, **118**, 8889–8935.
2 M. C. Tang, M. Y. Chan and V. W. Yam, Molecular Design of Luminescent Gold(III) Emitters as Thermally Evaporable and Solution-Processable Organic Light-Emitting Device (OLED) Materials, *Chem. Rev.*, 2021, **121**, 7249–7279.
3 W. R. Algar, M. Massey, K. Rees, R. Higgins, K. D. Krause, G. H. Darwish, W. J. Peveler, Z. Xiao, H. Y. Tsai, R. Gupta, K. Lix, M. V. Tran and H. Kim, Photoluminescent Nanoparticles for Chemical and Biological Analysis and Imaging, *Chem. Rev.*, 2021, **121**, 9243–9358.
4 J. Yu, Y. Rong, C. T. Kuo, X. H. Zhou and D. T. Chiu, Recent Advances in the Development of Highly Luminescent Semiconducting Polymer Dots and Nanoparticles for Biological Imaging and Medicine, *Anal. Chem.*, 2017, **89**, 42–56.
5 T. L. Mako, J. M. Racicot and M. Levine, Supramolecular Luminescent Sensors, *Chem. Rev.*, 2019, **119**, 322–477.
6 J. X. Wang, J. Yin, O. Shekhah, O. M. Bakr, M. Eddaoudi and O. F. Mohammed, Energy Transfer in Metal-Organic Frameworks for Fluorescence Sensing, *ACS Appl. Mater. Interfaces*, 2022, **14**, 9970–9986.
7 D. Di, A. S. Romanov, L. Yang, J. M. Richter, J. P. Rivett, S. Jones, T. H. Thomas, M. Abdi Jalebi, R. H. Friend, M. Linnolahti, M. Bochmann and D. Credgington, High-performance light-emitting diodes based on carbene-metal-amides, *Science*, 2017, **356**, 159–163.
8 B. Valeur and M. N. Berberan-Santos, *Molecular fluorescence: principles and applications*, Wiley-VCH, Weinheim, 2nd edn, 2012, pp. 66–67.

9 J. R. Albani, *Principles and Applications of Fluorescence Spectroscopy*, Wiley-VCH, Weinheim, 2007, Chapter 10, Fluorescence Quenching, pp. 139–159.

10 H. Schenk, M. Wolf, G. Mackh, U. Zehnder, W. Ossau, A. Waag and G. Landwehr, Influence of the negative thermal-expansion coefficient on the luminescence properties of (CdMnMg)Te, *J. Appl. Phys.*, 1996, **79**, 8704–8711.

11 S. A. Hodgson, S. J. Hunt, T. J. Sørensen, A. L. Thompson, E. M. Reynolds, S. Faulkner and A. L. Goodwin, Anomalous Thermal Expansion and Luminescence Thermochromism in Silver(I) Dicyanamide, *Eur. J. Inorg. Chem.*, 2016, **2016**, 4378–4381.

12 H. Zou, X. Yang, B. Chen, Y. Du, B. Ren, X. Sun, X. Qiao, Q. Zhang and F. Wang, Thermal Enhancement of Upconversion by Negative Lattice Expansion in Orthorhombic $Yb_2W_3O_{12}$, *Angew. Chem., Int. Ed.*, 2019, **58**, 17255–17259.

13 P. Dang, G. Li, X. Yun, Q. Zhang, D. Liu, H. Lian, M. Shang and J. Lin, Thermally stable and highly efficient red-emitting Eu^{3+}-doped $Cs_3GdGe_3O_9$ phosphors for WLEDs: non-concentration quenching and negative thermal expansion, *Light: Sci. Appl.*, 2021, **10**, 29.

14 H. Lv, P. Du, L. Luo and W. Li, Negative thermal expansion triggered anomalous thermal upconversion luminescence behaviors in Er^{3+}/Yb^{3+}-codoped $Y_2Mo_3O_{12}$ microparticles for highly sensitive thermometry, *Mater. Adv.*, 2021, **2**, 2642–2648.

15 L. Zhou, W. Wang, D. Xu, Z. Wang, Z. Yi, M. Wang and Z. Lu, Anti-thermal quenching of Eu^{3+} luminescence in negative thermal expansion $Zr(WO_4)_2$, *Ceram. Int.*, 2021, **47**, 34820–34827.

16 T. A. Mary, J. S. O. Evans, T. Vogt and A. W. Sleight, Negative Thermal Expansion from 0.3 to 1050 Kelvin in ZrW2O8, *Science*, 1996, **272**, 90–92.

17 Z. Liu, Q. Gao, J. Chen, J. Deng, K. Lin and X. Xing, Negative thermal expansion in molecular materials, *Chem. Commun.*, 2018, **54**, 5164–5176.

18 N. Shi, Y. Song, X. Xing and J. Chen, Negative thermal expansion in framework structure materials, *Coord. Chem. Rev.*, 2021, **449**, 214204.

19 Q. Li, K. Lin, Z. Liu, L. Hu, Y. Cao, J. Chen and X. Xing, Chemical Diversity for Tailoring Negative Thermal Expansion, *Chem. Rev.*, 2022, **122**, 8438–8486.

20 L. Chen, X. Chen, R. Ma, K. Lin, Q. Li, J. P. Lang, C. Liu, K. Kato, L. Huang and X. Xing, Thermal Enhancement of Luminescence for Negative Thermal Expansion in Molecular Materials, *J. Am. Chem. Soc.*, 2022, **144**, 13688–13695.

21 H. C. Zhou, J. R. Long and O. M. Yaghi, Introduction to metal-organic frameworks, *Chem. Rev.*, 2012, **112**, 673–674.

22 H. C. Zhou and S. Kitagawa, Metal-organic frameworks (MOFs), *Chem. Soc. Rev.*, 2014, **43**, 5415–5418.

23 H. Furukawa, K. E. Cordova, M. O'Keeffe and O. M. Yaghi, The chemistry and applications of metal-organic frameworks, *Science*, 2013, **341**, 1230444.

24 W. Lu, Z. Wei, Z. Y. Gu, T. F. Liu, J. Park, J. Park, J. Tian, M. Zhang, Q. Zhang, T. Gentle 3rd, M. Bosch and H. C. Zhou, Tuning the structure and function of metal-organic frameworks via linker design, *Chem. Soc. Rev.*, 2014, **43**, 5561–5593.

25 A. Schoedel, M. Li, D. Li, M. O'Keeffe and O. M. Yaghi, Structures of Metal-Organic Frameworks with Rod Secondary Building Units, *Chem. Rev.*, 2016, **116**, 12466–12535.

26 L. Sun, M. G. Campbell and M. Dinca, Electrically Conductive Porous Metal-Organic Frameworks, *Angew. Chem., Int. Ed.*, 2016, **55**, 3566–3579.

27 C. Hua, P. W. Doheny, B. Ding, B. Chan, M. Yu, C. J. Kepert and D. M. D'Alessandro, Through-Space Intervalence Charge Transfer as a Mechanism for Charge Delocalization in Metal-Organic Frameworks, *J. Am. Chem. Soc.*, 2018, **140**, 6622–6630.

28 W. P. Lustig, S. Mukherjee, N. D. Rudd, A. V. Desai, J. Li and S. K. Ghosh, Metal-organic frameworks: functional luminescent and photonic materials for sensing applications, *Chem. Soc. Rev.*, 2017, **46**, 3242–3285.

29 C. S. Coates and A. L. Goodwin, How to quantify isotropic negative thermal expansion: magnitude, range, or both?, *Mater. Horiz.*, 2019, **6**, 211–218.

30 J. H. Cavka, S. Jakobsen, U. Olsbye, N. Guillou, C. Lamberti, S. Bordiga and K. P. Lillerud, A new zirconium inorganic building brick forming metal organic frameworks with exceptional stability, *J. Am. Chem. Soc.*, 2008, **130**, 13850–13851.

31 Y. Bai, Y. Dou, L. H. Xie, W. Rutledge, J. R. Li and H. C. Zhou, Zr-based metal-organic frameworks: design, synthesis, structure, and applications, *Chem. Soc. Rev.*, 2016, **45**, 2327–2367.

32 H. Liu, M. Cheng, Y. Liu, G. Zhang, L. Li, L. Du, B. Li, S. Xiao, G. Wang and X. Yang, Modified UiO-66 as photocatalysts for boosting the carbon-neutral energy cycle and solving environmental remediation issues, *Coord. Chem. Rev.*, 2022, **458**, 214428.

33 M. Bonneau, C. Lavenn, J. J. Zheng, A. Legrand, T. Ogawa, K. Sugimoto, F. X. Coudert, R. Reau, S. Sakaki, K. I. Otake and S. Kitagawa, Tunable acetylene sorption by flexible catenated metal-organic frameworks, *Nat. Chem.*, 2022, **14**, 816–822.

34 J. Hao, X. Xu, H. Fei, L. Li and B. Yan, Functionalization of Metal-Organic Frameworks for Photoactive Materials, *Adv. Mater.*, 2018, **30**, e1705634.

35 D. X. Xue, Y. Belmabkhout, O. Shekhah, H. Jiang, K. Adil, A. J. Cairns and M. Eddaoudi, Tunable Rare Earth fcu-MOF Platform: Access to Adsorption Kinetics Driven Gas/Vapor Separations via Pore Size Contraction, *J. Am. Chem. Soc.*, 2015, **137**, 5034–5040.

36 P. Yi, H. Huang, Y. Peng, D. Liu and C. Zhong, A series of europium-based metal organic frameworks with tuned intrinsic luminescence properties and detection capacities, *RSC Adv.*, 2016, **6**, 111934–111941.

37 T. Xia, Y. Wan, Y. Li and J. Zhang, Highly Stable Lanthanide Metal-Organic Framework as an Internal Calibrated

Luminescent Sensor for Glutamic Acid, a Neuropathy Biomarker, *Inorg. Chem.*, 2020, **59**, 8809–8817.

38 J. Zhou, H. Li, H. Zhang, H. Li, W. Shi and P. Cheng, A Bimetallic Lanthanide Metal-Organic Material as a Self-Calibrating Color-Gradient Luminescent Sensor, *Adv. Mater.*, 2015, **27**, 7072–7077.

39 Y. Cui, B. Chen and G. Qian, Lanthanide metal-organic frameworks for luminescent sensing and light-emitting applications, *Coord. Chem. Rev.*, 2014, **273–274**, 76–86.

40 B. Chen, Y. Yang, F. Zapata, G. Lin, G. Qian and E. B. Lobkovsky, Luminescent Open Metal Sites within a Metal–Organic Framework for Sensing Small Molecules, *Adv. Mater.*, 2007, **19**, 1693–1696.

41 T.-W. Duan and B. Yan, Hybrids based on lanthanide ions activated yttrium metal–organic frameworks: functional assembly, polymer film preparation and luminescence tuning, *J. Mater. Chem. C*, 2014, **2**, 5098–5104.

42 X. Yang, X. Lin, Y. Zhao, Y. S. Zhao and D. Yan, Lanthanide Metal-Organic Framework Microrods: Colored Optical Waveguides and Chiral Polarized Emission, *Angew. Chem., Int. Ed.*, 2017, **56**, 7853–7857.

43 Z. Gao, B. Xu, T. Zhang, Z. Liu, W. Zhang, X. Sun, Y. Liu, X. Wang, Z. Wang, Y. Yan, F. Hu, X. Meng and Y. S. Zhao, Spatially Responsive Multicolor Lanthanide-MOF Heterostructures for Covert Photonic Barcodes, *Angew. Chem., Int. Ed.*, 2020, **59**, 19060–19064.

44 M. J. Neufeld, H. Winter, M. R. Landry, A. M. Goforth, S. Khan, G. Pratx and C. Sun, Lanthanide Metal-Organic Frameworks for Multispectral Radioluminescent Imaging, *ACS Appl. Mater. Interfaces*, 2020, **12**, 26943–26954.

45 L. V. Meyer, F. Schonfeld and K. Muller-Buschbaum, Lanthanide based tuning of luminescence in MOFs and dense frameworks-from mono- and multimetal systems to sensors and films, *Chem. Commun.*, 2014, **50**, 8093–8108.

46 H. Q. Yin, X. Y. Wang and X. B. Yin, Rotation Restricted Emission and Antenna Effect in Single Metal-Organic Frameworks, *J. Am. Chem. Soc.*, 2019, **141**, 15166–15173.

47 X. P. Wu, L. Gagliardi and D. G. Truhlar, Cerium Metal-Organic Framework for Photocatalysis, *J. Am. Chem. Soc.*, 2018, **140**, 7904–7912.

48 L. B. McCusker, R. B. Von Dreele, D. E. Cox, D. Louër and P. Scardi, Rietveld refinement guidelines, *J. Appl. Crystallogr.*, 1999, **32**, 36–50.

49 M. Karabacak, M. Cinar, Z. Unal and M. Kurt, Temperature and Phase Behavior of Infrared Intensities: The Poly(methylene) Chain, *J. Phys. Chem.*, 1986, **90**, 5623–5630.

50 A. B. Andreeva, K. N. Le, L. Chen, M. E. Kellman, C. H. Hendon and C. K. Brozek, Soft Mode Metal-Linker Dynamics in Carboxylate MOFs Evidenced by Variable-Temperature Infrared Spectroscopy, *J. Am. Chem. Soc.*, 2020, **142**, 19291–19299.

51 M. Kandiah, S. Usseglio, S. Svelle, U. Olsbye, K. P. Lillerud and M. Tilset, Post-synthetic modification of the metal–organic framework compound UiO-66, *J. Mater. Chem.*, 2010, **20**, 9848–9851.

52 L. Valenzano, B. Civalleri, S. Chavan, S. Bordiga, M. H. Nilsen, S. Jakobsen, K. P. Lillerud and C. Lamberti, Disclosing the Complex Structure of UiO-66 Metal Organic Framework: A Synergic Combination of Experiment and Theory, *Chem. Mater.*, 2011, **23**, 1700–1718.

53 K. Tan, H. Pandey, H. Wang, E. Velasco, K. Y. Wang, H. C. Zhou, J. Li and T. Thonhauser, Defect Termination in the UiO-66 Family of Metal-Organic Frameworks: The Role of Water and Modulator, *J. Am. Chem. Soc.*, 2021, **143**, 6328–6332.